Chemistry and Physics of Lipids 233 (2020) 104991

Contents lists available at ScienceDirect

Chemistry and Physics of Lipids

journal homepage: www.elsevier.com/locate/chemphyslip

Single-lipid dynamics in phase-separated supported lipid bilayers

Xinxin Woodward, Christopher V. Kelly *

Department of Physics and Astronomy, Wayne State University, Detroit, MI, United States

ARTICLE INFO

Keywords:
Supported lipid bilayers
Diffusion
Aggregation
Single-particle tracking
Coexisting liquid phases

ABSTRACT

Phase separation is a fundamental organizing mechanism on cellular membranes. Lipid phases have complex dependencies on the membrane composition, curvature, tension, and temperature. Lipid diffusion rates vary by up to ten-fold between liquid-disordered (L_d) and liquid-ordered (L_o) phases depending on the membrane composition, measurement technique, and the surrounding environment. This manuscript reports the lipid diffusion on phase-separated supported lipid bilayers (SLBs) with varying temperature, composition, and lipid phase. Lipid diffusion is measured by single-particle tracking (SPT) and fluorescence correlation spectroscopy (FCS) via custom data acquisition and analysis protocols that apply to diverse membranes systems. Traditionally, SPT is sensitive to diffuser aggregation, whereas the diffusion rates reported by FCS are unaffected by the presence of immobile aggregates. Within this manuscript, we report (1) improved single-particle tracking analysis of lipid diffusion, (2) comparison and consistency between diffusion measurement methods for non-Brownian diffusers, and (3) the application of these methods to measure the phase, temperature, and composition dependencies in lipid diffusion. We demonstrate improved SPT analysis methods that yield consistent FCS and SPT diffusion results even when most fluorescent lipids are frequently confined within aggregates within the membrane. With varying membrane composition and temperature, we demonstrate differences in diffusion between the L_d and L_o phases of SLBs.

1. Introduction

Cell plasma membranes are often modeled as a two dimensional fluid with lipid phase separation (Pike, 2006; Pralle et al., 2000; Simons and Ikonen, 1997). Lipid phases are hypothesized to be critical for cell functions such as protein sorting, cell signaling, and membrane budding (Fessler and Parks, 2011; Hurley et al., 2010; Simons and Toomre, 2000). Model membranes enable detailed analyses of coexisting liquid phases by connecting the membrane composition with biophysical observables, such as viscosity, bilayer thickness, and fluctuation analyses (Kiessling et al., 2015; Veatch and Keller, 2005). However, anomalous diffusion, lipid confinement, and nanodomains complicate the measurement of the membrane properties while revealing heterogeneity in lipid behavior.

Model membranes can phase separate into a liquid-ordered phase (L_o) and a liquid-disordered phase (L_d) when composed of a mixture of three lipid types: a phospholipid with a high melting temperature, a phospholipid with low melting temperature, and a sterol (Veatch and Keller, 2002). Lipids with a high melting temperature tend to have longer and more saturated acyl tails while concentrating in the L_o phase. Lipids with a low melting temperature commonly have shorter, unsaturated tails while concentrating in the L_d phase. The most used sterol in model membranes is cholesterol, which slightly concentrates within the L_o phase. Additionally, separate condensed complexes composed of cholesterol and DPPC may further affect the lipid dynamics, but do not appear with diffraction-limited microscopy (McConnell and Radhakrishnan, 2003; Radhakrishnan and McConnell, 2005).

Phase-separated model membranes commonly contain an L_o phase that is up to 0.8 nm ticker (Bleecker et al., 2016; Chiantia et al., 2006b, 2006a; Lin et al., 2007), with up to 3x greater bending rigidity (Baumgart et al., 2003; Dimova, 2014; Gracià et al., 2010; Kollmitzer et al., 2015), and up to 10x greater effective viscosity (Kahya et al., 2003; Scherfeld et al., 2003) than the L_d phase. Increasing the sample temperature shortens the tie-lines and causes the L_o and L_d phases to become

Abbreviations: DiPhyPC, diphytanoyl-phosphatidylcholine; DPPC, dipalmitoyl-phosphatidylcholine; DPPE-TR, dipalmitoyl-phosphoethanolamine-Texas Red; FCS, fluorescent correlation spectroscopy; GUV, giant unilamellar vesicle; *Lα*, liquid phase of a one-component membrane; *Ld*, liquid-disordered phase; *Lo*, liquid-ordered phase; *L*, intermediate, homogeneous liquid phase; MSD, mean squared displacement; *N*, number of localizations per aggregate; POPC, palmitoyl-oleoyl-phosphatidylcholine; SLB, supported lipid bilayer; SPT, single-particle tracking.

* Corresponding author.
E-mail address: cvkelly@wayne.edu (C.V. Kelly).

https://doi.org/10.1016/j.chemphyslip.2020.104991
Received 28 May 2020; Received in revised form 2 October 2020; Accepted 6 October 2020
Available online 26 October 2020

more similar in composition and behavior (Fig. 1). If the temperature is above the miscibility transition temperature (T_m), a single liquid phase (L) exists. The phases reemerge when the membrane temperature drops below T_m due to an interplay of phase nucleation and growth dynamics. With increasing temperature, the diffusion rate of the lipids increases (Almeida et al., 1992; Bag et al., 2014; Jacobson et al., 1981; Tamm, 1988; Wu et al., 1977). If the temperature of a phase-separated membrane is increased above T_m, then the two populations of tracer lipids become a single population (Filippov et al., 2004; Lindblom et al., 2006).

Varying membrane preparations and analysis methods provide differing resolution of heterogeneous tracer populations with non-Brownian diffusion. Lipids may form clusters and demonstrate confined motion due to interactions with the supporting substrates (Beckers et al., 2020; Hsieh et al., 2014; Spillane et al., 2014; Wawrezinieck et al., 2005), nonspecific lipid-lipid interactions (Jan Akhunzada et al., 2019; Scherer et al., 2015; Spillane et al., 2014), specific condensed complexes (McConnell and Radhakrishnan, 2003; Radhakrishnan and McConnell, 2005), lipid crosslinking (Štefl et al., 2012), incomplete bilayer formation (Coker et al., 2019), and phase-associated nanodomains (Sodt et al., 2014; Wu et al., 2016). For example, even bilayers with ≤2 mol% GM1 form isolated nanodomains within larger liquid lipid phase regions (Sun et al., 2015; Yuan et al., 2002; Yuan and Johnston, 2001). Robust methods to characterize lipid clustering or aggregation are needed to resolve the varying modes of diffusion and influences of lipid behavior.

Two complementary techniques to study single-molecule diffusion are fluorescence correlation spectroscopy (FCS) and single-particle tracking (SPT). Although FCS and SPT measure molecular mobility and report the same results under ideal conditions, significant differences in the reported results are found when non-Brownian diffusion, multiple populations of diffusers, or a light-sensitive sample are present (Harwardt et al., 2018). Unlike SPT, the diffusion rates reported by FCS do not account for immobile tracers, and FCS is insensitive to the identification of subpopulations of diffusers (Guo et al., 2012). Understanding the source of the differences in results from FCS and SPT can be key to understanding the complex molecular diffusion in a sample.

This manuscript reports the use of optimized analysis procedures to identify non-Brownian diffusers, map the lipid diffusion rate across a sample, and report on the composition-and temperature-dependence in tracer lipid diffusion within phase-separated SLBs. Initial differences between FCS and SPT results were associated with the presence of aggregates in DiPhyPC-containing SLBs. Aggregate identification and data culling were performed to study single-lipid diffusion via SPT upon which consistency was demonstrated between FCS and SPT. SPT was performed with both mean squared displacement (MSD) and single-step-length Rayleigh distributions. In all conditions, faster diffusion was observed for higher temperatures, and greater differences between coexisting phases were observed when the tie-lines were expected to be longer. The protocols developed here are directly applicable to identifying the non-Brownian diffusion, identifying sub-populations of diffusers, and mapping the lateral heterogeneities in effective membrane viscosities, such as those created by nanoscale curvature (Woodward and Kelly, 2020).

2. Materials and methods

2.1. GUV formation

Quasi-one component bilayers composed of diphytanoyl-phosphatidylcholine (DiPhyPC; Avanti Polar Lipids) or palmitoyl-oleoyl-phosphatidylcholine (POPC, Avanti Polar Lipids) were used to examine the liquid phase of a quasi-one-component membrane (L_α) at room temperature (Fig. 1A). DiPhyPC was used more frequently than POPC in this manuscript because DiPhyPC contains saturated, branched acyl tails that provide both resistance to oxidization and a low melting transition temperature <-120 °C (Lindsey et al., 1979). DiPhyPC was combined with dipalmitoyl-phosphatidylcholine (DPPC; Avanti Polar Lipids) and cholesterol (Avanti Polar Lipids) to study phase-separated SLBs. A fluorescent lipid, dipalmitoyl-phosphoethanolamine-Texas Red (DPPE-TR, Life Technologies), was used to label the L_d domain with a total concentration of 0.1 mol% in all membranes. We used three membrane compositions of 1:0:0, 2:2:1, and 1:1:2 molar ratios of DiPhyPC:DPPC:cholesterol. The buffers were created from Milli-Q water with a resistivity of 18 mΩ. All other chemicals were bought from Sigma Aldrich and used without further purification.

All samples were created by the fusion of giant unilaminar vesicles (GUVs) on a glass coverslip. Our GUV making protocol was adapted from previous reports (Veatch, 2007). Lipids were combined at the desired ratio in chloroform with a concentration of 5 mg/mL and dried onto electrically conducting indium tin oxide-coated glass plates. A trimmed silicon sheet was added between the plates and stabilized by clips to create an incubation chamber. The chamber was filled with 200 mM sucrose and exposed to an AC voltage with V_{rms} of 3 V at 10 Hz for 1 h at

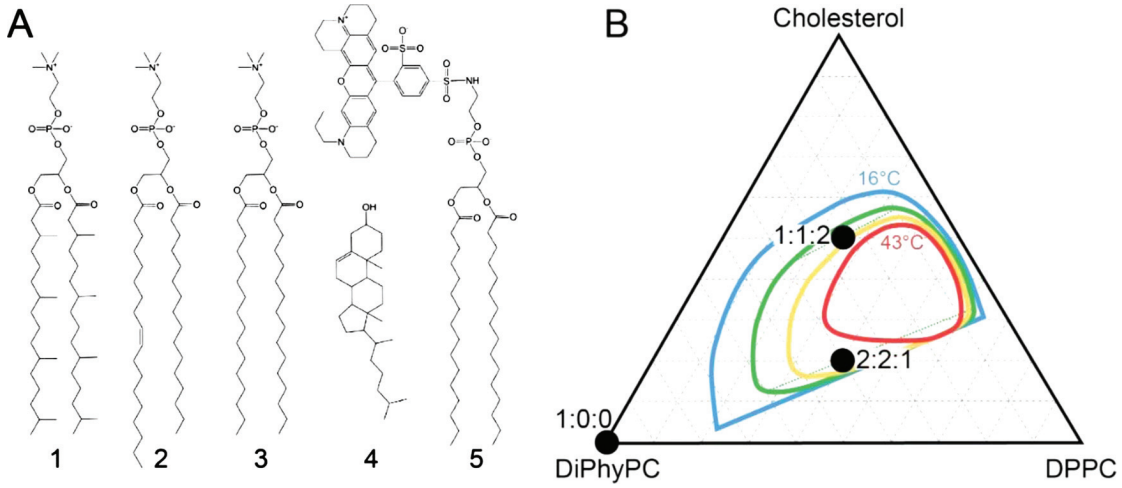

Fig. 1. (A) The lipids used in this study include DiPhyPC (1), POPC (2), DPPC (3), cholesterol (4), and DPPE-TR (5). (B) Mixtures of DiPhyPC, DPPC, and cholesterol display two coexisting liquid phases within the indicated regions that vary with temperature. The DiPhyPC:DPPC:cholesterol molar ratios used in this study are shown (*black dots*). The 16 °C (*blue*) and 43 °C (*red*) phase boundaries were measured previously in GUVs (Veatch et al., 2006). The approximate boundary of liquid phase coexistence at 25 °C (*green*) and 34 °C (*yellow*) for SLBs are also shown. The approximate tie-line at 25 °C (*green dotted*) is longer for the composition of 2:2:1 than 1:1:2 molar ratios, indicating a greater similarity between the liquid phases with increased cholesterol.

55 °C. The resulting GUV solution had a concentration of 13 mg lipids per mL and was stored at 55 °C until use. The GUVs were used within two days.

2.2. Substrate preparation

All SLBs were formed and imaged on 35 mm diameter glass-bottom dishes (MatTek). Dishes were initially rinsed with ethanol, dried by a nitrogen gas stream, and placed in air plasma (Harrick Plasma) for 10 s to create a hydrophilic surface. 20 μL of 50 mM $CaCl_2$ was deposited on the dish and dried on a hot plate at 35 °C for 10 min. At least three SLB patches from each of two GUV batches were used for each reported condition.

2.3. Supported-lipid bilayer formation

GUVs were cooled to 4 °C before SLB formation. 5 μL of 4 °C GUVs and 50 μL of 4 °C Milli-Q water were sequentially deposited on the room temperature glass-bottom dish. The dishes were maintained at 4 °C for 15 min before gently rinsing with 5 mL of 4 °C 200 mM sucrose. We note that the dishes were at room temperature before the addition of the GUV solution. If the sample dish was cooled to 4 °C before GUV deposition, the condensation on glass reduced GUV fusion. The resulting SLB patches had lipid phase domains with similar size and shape, as seen on the GUVs before fusion (Fig. 2).

2.4. Temperature control

A Peltier temperature control dish holder (QE-1HC, Warner Instruments) was used with custom insulated dish cover, LabVIEW control, and a thermocouple holder. The thermocouple was positioned <0.5 mm above the center of the glass coverslip for real-time temperature feedback. The temperature was changed by 0.5 °C/min and remained at each set temperature for ≥30 min before data acquisition. The dish holder was initially set to 10 °C. When the temperature was set to 10 °C, 30 °C, or 45 °C, the resulting measured temperature was 17 ± 3 °C, 27 ± 1 °C, and 37 ± 1 °C, respectively. The dishes were never heated above 45 °C due to limitations in our optical system.

2.5. Single-fluorophore imaging

The optical setup included an inverted IX83 microscope with a 100x, 1.49 NA objective (Olympus), a 2x emission path magnification (Opto-Split, Cairn Research), and an iXon 897-Ultra EMCCD camera (Andor Technology). A Hg lamp with an excitation filter (BrightLine single-band, Semrock) provided wide-field fluorescence illumination for the diffraction-limited images. CUBE diode lasers with wavelengths of 405 and 488 nm (Coherent) and a 561 nm Sapphire laser (Coherent) were used for single-fluorophore excitation. The laser light passed through a clean-up filter (zet405/488/561/647x, Chroma Technology), reflected from a quad-band dichroic mirror (zt405/488/561/647rpc, Chroma Technology), and transmitted into the objective to excite the sample. The fluorescence emission was isolated via emission filters (BrightLine single-band filter, Semrock) and a 4-band notch laser filter (zet405/488/561/640 m, Chroma Technology). SOLIS software (Andor Technology) was used to acquire images and movies with a 128-pixel x 128-pixel region of interest in the kinetic read mode and an EM gain of 150. Videos of single-fluorophores blinking were acquired at 537 Hz with ≥20,000 frames per sample.

2.6. Single-fluorophore localization

The videos of optically isolated fluorescent lipids were analyzed with the Fiji plug-in ThunderSTORM (Ovesný et al., 2014; Schindelin et al., 2012). Via ThunderSTORM, each bright spot in the movies was fit with a 2D Gaussian function to identify the location, intensity, fit width, localization uncertainty (σ_r), and brightness of each fluorophore. Only the fluorophore localizations with intensity >100 photons, Gaussian fit width >15 nm, and σ_r <45 nm were kept for further analysis. ThunderSTORM reported $\sigma_r = 24 \pm 1$ nm for the remaining localizations.

2.7. Aggregate removing method

Aggregated localizations were identified via spatial autocorrelation analysis. The localizations were two-dimensionally histogrammed to create a reconstructed image, $I(\vec{r})$. Spatial autocorrelation functions, $g_s(r)$, were calculated with fast Fourier transforms (FFTs) according to

$$g_s(r) = \frac{\left\langle FFT^{-1}\left(\left|FFT(I(\vec{r}))\right|^2\right)\right\rangle_\theta}{\rho^2} \quad (1)$$

for which ρ is the average localization density, and averaging was performed over the azimuthal angle (θ), as done previously (Veatch et al., 2012). We calculated g_s from the experimental and simulated localization data to yield g_{exp} and g_{sim}, respectively. The simulated localizations were randomly distributed over the same membrane shape that was observed experimentally to provide an aggregate-free normalization.

The average aggregate size and the number of localizations per aggregate (N) were calculated by identifying the exponential decay length scale and via Eq. 2, respectively, as done previously (Shelby et al., 2013).

$$N = \int\left(\frac{g_{exp}(r)}{g_{sim}(r)} - 1\right) r dr \quad (2)$$

Aggregate removal included the grouping of all single-fluorophore localizations to 3D voxels of time and xy-position. When the number of localizations per voxel was above a density threshold (ρ_{th}), the localizations were assessed to be part of an aggregate and removed from subsequent analysis. ρ_{th} was varied to remove between 0–90% of all localizations for testing. For each ρ_{th}, the remaining experimental localizations were used to calculate N. Decreasing ρ_{th} resulted in decreasing N, as expected. The ρ_{th} value that was chosen for aggregate-

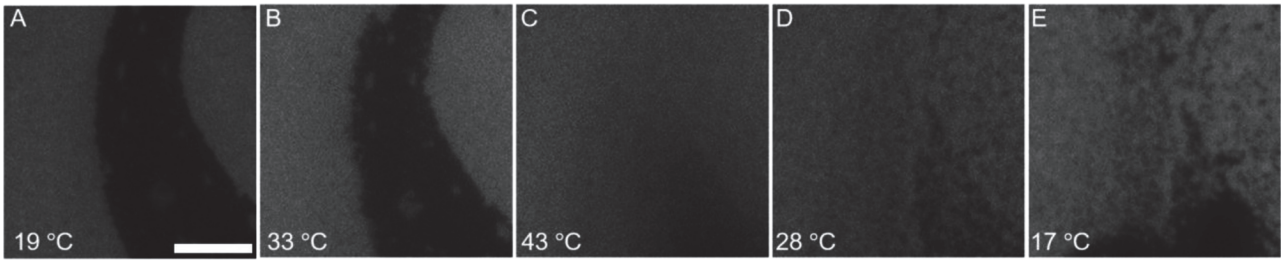

Fig. 2. The coexisting phases in an SLB with a 1:1:2 molar ratio of DiPhyPC:DPPC:cholesterol mix upon heating and reform upon cooling. Below 35 °C, the bilayer is phase-separated into L_d (*bright*) and L_o (*dim*) phases due to partitioning of the fluorescent DPPE-TR into the L_d phase. These panels are shown in the order in which they were acquired with 50 min between frames. Scale bar, 5 μm.

removed diffusion analysis was the maximum ρ_{th} value that yielded $N < 3$.

2.8. Single-molecule trajectory analysis

The remaining localizations after aggregate removal were linked through u-track (Jaqaman et al., 2008) with a maximum linking radius of 400 nm. Trajectories with more steps yielded a slower diffusion compared to shorter trajectories, as observed previously (Saxton, 1997). The longer trajectories were possibly from oligomers, as would be expected to have slower diffusion than single lipids. Therefore, trajectories longer than 32 steps were removed from all diffusion studies whenever aggregates were removed. These aggregate and long-trajectory removal methods resulted in the average trajectory consisting of 6 ± 4 steps.

2.8.1. Rayleigh distribution analysis

The single-fluorophore step lengths (ν) were fit to Rayleigh distribution (R) to find the diffusion coefficient (D_{fit}), as done previously (Cheney et al., 2017; Kabbani et al., 2020, 2017; Kabbani and Kelly, 2017b; Knight et al., 2010; Woodward et al., 2018),

$$R(\nu) = \frac{\nu}{2D_{fit}\Delta t} e^{-\frac{\nu^2}{4D_{fit}\Delta t}} \quad (3)$$

D_{fit} was corrected for imaging blur and localization uncertainty to yield the diffusion coefficient from this single-step length analysis (D_{RD}) (Berglund, 2010; Lagerholm et al., 2017; Qian et al., 1991).

$$D_{RD} = \frac{D_{fit} - \frac{\sigma_r^2}{2\Delta t}}{1 - \frac{t_{exp}}{3\Delta t}} \quad (4)$$

The difference between the D_{fit} and D_{RD} values depends on the single-frame exposure time (t_{exp}), the time between frames (Δt), and localization uncertainty (σ_r) exported by ThunderSTORM.

2.8.2. Mean squared displacement analysis

The MSD as a function of Δt was calculated for all samples (Wu et al., 1977). D_{MSD} was found by fitting the first two time points (*i.e.,* $\Delta t = 1.9$ and 3.8 ms) of the localization uncertainty and image blur-corrected MSD versus Δt,

$$\text{MSD} = \frac{10}{3} D_{MSD}\Delta t + 2\sigma_r^2 \quad (5)$$

By using σ_r exported from ThunderSTORM rather than incorporating it as an unknown in the fitting routine, D_{MSD} and D_{RD} could be directly compared without using the y-intercept of the MSD versus Δt fit before performing the Rayleigh distribution analysis.

2.9. Fluorescence correlation spectroscopy

FCS was performed with a customized IX71 microscope and a 40x, 1.3 NA objective (Olympus). The excitation was a super-continuum fiber laser (SC-Pro, YSL photonics). The long-wavelength component (>650 nm) was removed before the light was chromatically filtered (BrightLine FF01-561/14-25, Semrock), expanded, and focused by the microscope objective onto the sample. The laser power entering the microscope objective was 1.6 μW. A beam waist of 180 ± 20 nm was formed on the SLB. The fluorescence emission was filtered (ZET442/514/561 m, Chroma) and collected on an sCMOS camera (Zyla, Andor Technology). Each camera frame was acquired for 1 ms at a 900 Hz frame rate during repeated 10-sec acquisitions. The mean intensity of each camera frame was calculated to be the intensity (I) of the emission. The temporal autocorrelation function (g_{FCS}) was calculated from intensity versus time according to

$$g_{FCS}(\tau) = \frac{FFT^{-1}(|FFT(I(t))|^2)}{<I(t)>^2} \quad (6)$$

where <> here represents the time average. All FCS experiments were performed at room temperature (25 ± 2 °C). Z-scan FCS was performed to optimize the focus and to ensure the minimum beam waist was consistently obtained. Five locations from each of two sample dishes were measured for each condition.

3. Results

3.1. Creating phase-separated SLBs

We created phase-separated SLBs with 1:1:2 and 2:2:1 molar ratios of DiPhyPC:DPPC:cholesterol. The phases were identified by the differential partitioning of the fluorescent lipid, DPPE-TR, such that higher concentrations of DPPE-TR were in more disordered phases. All phases appeared to be liquid in GUVs with rapid diffusion and merging of the phases. The phases on the SLBs were similar in size and shape to those on the GUVs but immobile on the time scale on our experiments. The varying composition between GUVs within a single preparation resulted in varying T_m and DPPE-TR partition coefficients for the separate SLB patches in each sample dish. The 1:1:2 SLBs had higher cholesterol content and a lower T_m than the 2:2:1 SLBs (Fig. 1B).

During the optimization of the SLB formation method, the importance of deposition temperature, buffer, and substrate preparation were each noted. Our initial trials yielded SLBs that contained membrane defects (*i.e.,* holes in the bilayer or abundant fused nanoscale vesicles) or did not maintain the large-scale phase separation that was seen on the GUVs. The keys parameters for high-quality SLB formation were to cool the GUVs and the buffers before GUV fusion with trace $CaCl_2$, as detailed in the Methods section. For example, when we directly transferred GUVs from the 55 °C incubator to the room-temperature glass coverslip, the SLBs consistently demonstrated a phase separation with the L_d phase at the center and L_o phase at the perimeter of the SLB patch. SLB formation from GUV fusion in the presence of sucrose solution resulted in smoother SLBs than when an ionic buffer was used; vesicles of sub-micron diameter covered the SLB patches when phosphate buffered saline was present during SLB formation. After the SLB formation, the buffers could be exchanged as needed without significant change to the quality of the SLB.

3.2. Temperature-induced phase changes

A convenient method for dynamically varying the phase separation in a single sample was to change the sample temperature. As the temperature was increased, the fluorescence emission from the L_d and L_o phases became more similar (Fig. 2), as seen previously (Gunderson and Honerkamp-Smith, 2018). This is consistent with an increasing temperature resulting in less compositional difference and a shorter tie-line separating the coexisting phases. When the temperature was held slightly above T_m, the two phases mix into a single liquid phase (L) with composition and material properties between the L_d and L_o phases. Prior reports vary with labeling the warm, homogeneous liquid phase of mixed lipids *as* L_o (Feigenson, 2009, 2006) or leaving it unlabeled (Ackerman and Feigenson, 2015; Heberle and Feigenson, 2011); within this manuscript, we use the label L as a representation of its intermediate qualities of this homogenous, multicomponent liquid phase (Veatch and Keller, 2005) while reserving the L_α designation for the designation of a lipid phase of the single-component liquid membrane.

The majority of SLBs with a 1:1:2 molar ratio of DiPhyPC:DPPC: cholesterol demonstrated phase mixing with a uniform fluorescence emission across the sample after the temperature was maintained at 40 °C for 30 min. However, the large domains of area >100 μm^2 were unable to mix fully during this time and maintained partial phase separation throughout our observation (Fig. 2C).

As the temperature was decreased from 40 °C to 30 °C for 1:1:2 SLBs, domains became optically identifiable and enlarged within 5 min.

However, the domains did not grow larger than nanoscale in diameter during our 30 min of observation at 30 °C or colder temperatures (Fig. 2D). The locations of new domain formation upon cooling were typically random and not dependent on the prior domain locations. However, large domains that were not fully mixed at 40 °C demonstrated L_o phase domains preferentially forming at the prior L_o regions upon cooling.

SLBs with composition 2:2:1 molar ratio of DiPhyPC:DPPC:cholesterol had T_m above 40 °C. Even after 120 min at 40 °C, the L_o and L_d phases boundaries were always clearly defined, which is consistent with a large tie-line separating the L_o and L_d phases.

3.3. Aggregate identification and removal

The single-molecule localization data were reconstructed as super-resolution images with Voronoi diagrams. Voronoi diagrams are created by dividing the imaged area into polygons such that each polygon represents the area of the image that is closest to a particular single-molecule localization. The polygon area represents the localization density without binning biases and was colored accordingly. The lateral variations across the Voronoi images of DPPE-TR localizations in POPC bilayers were consistent with random sampling density variations expected from the total number of localizations acquired (Fig. 3a). However, non-random distributions of DPPE-TR localizations were observed in all DiPhyPC-containing bilayers (Fig. 3b). Unlike the super-resolution images of the POPC bilayer, the super-resolution images with DiPhyPC showed <70 nm diameter aggregates of dense localizations.

Quantification of the aggregates was performed by calculating the spatial autocorrelation (g_{exp}) (Eq. 1). Random distributions of localizations yield $g_{exp} = 1$ with no increased probability of finding a localization in the proximity of other localizations. The presence of aggregates, however, appears in g_{exp} because localizations are more likely to be found close together. g_{exp} reveals the size and density of the average aggregate. The area under g_{exp} measures the number of localizations in the average aggregate compared to the sample average localization density. The aggregates within DiPhyPC-containing SLBs were 63 ± 13 nm diameter and contained $N = 20 \pm 1$ localizations each for all compositions tested (Fig. 3D and E).

A threshold density of localizations (ρ_{th}) was used to identify and remove aggregation. All localizations from the regions of the SLB that displayed localization rates above ρ_{th} were culled to provide an aggregate-free assessment of the single-lipid diffusion. Smaller values of ρ_{th} resulted in smaller values of N from the remaining localizations (Eq. 2). ρ_{th} was set to be the largest value that provided $N \leq 3$ for further analysis. ρ_{th} varied between 430–82000 localizations μm^{-2} s^{-1} depending on the density of the aggregates, the experiment duration, the laser power, and the sample's fluorophore concentration. Additionally, any localizations that were linked to be a trajectory lasting more than 32 steps was determined to be an outlier and removed from further analysis. After the aggregates and long trajectories were removed, D_{MSD} increased in DiPhyPC SLBs by (1.7 ± 0.6)x at 14 °C and (1.4 ± 0.3)x at 28 °C (Fig. 3F). Additional methods of identifying and removing aggregates were also tested, including culling based on the localization brightness, the localization size, the trajectory step lengths, or the trajectory confinement; however, none of these aggregate characteristics proved to sufficiently robust for single-aggregate identification.

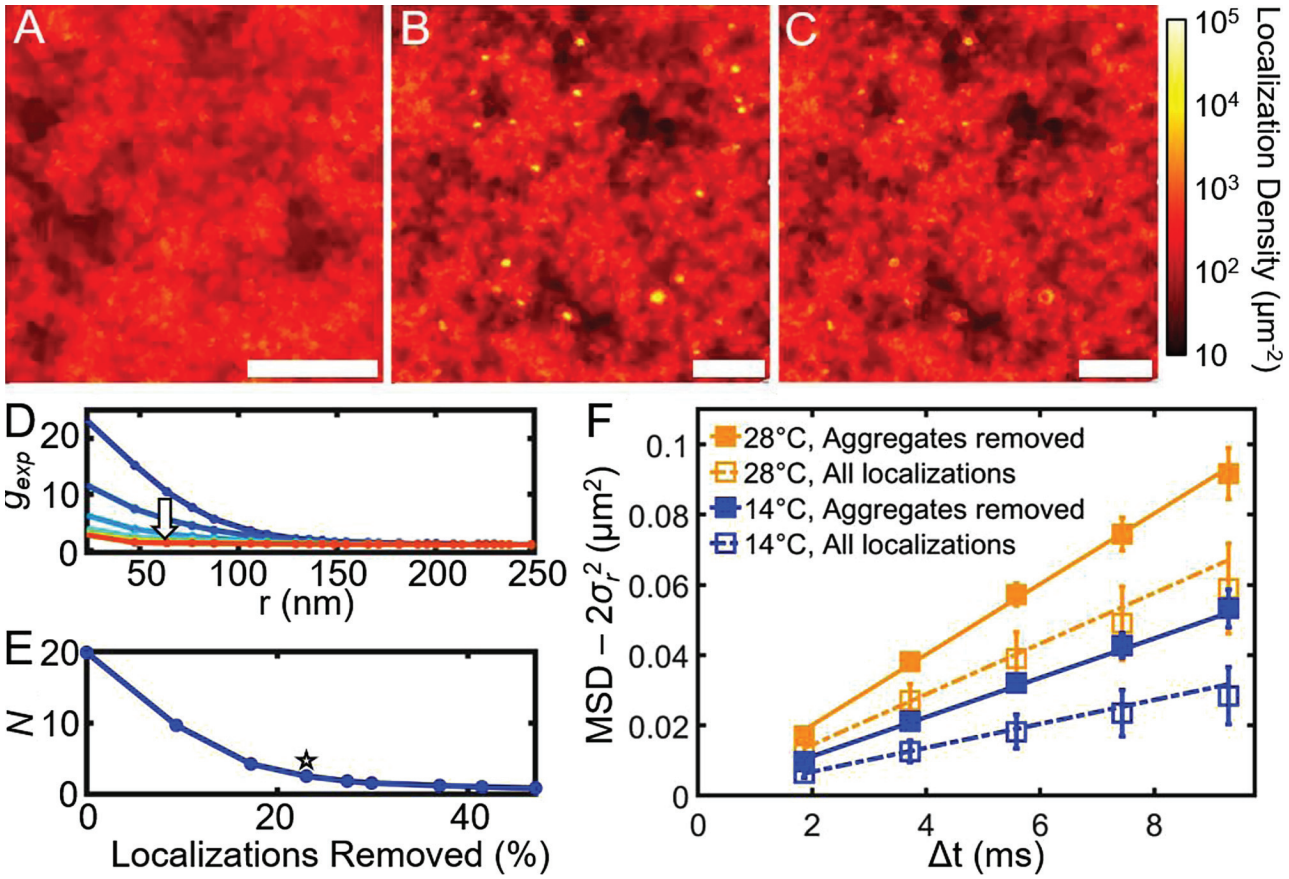

Fig. 3. Aggregation was observed in SLBs with DiPhyPC but not POPC. A Voronoi diagram of DPPE-TR localizations in a POPC bilayer at 25 °C shows randomly distributed localizations (A). Voronoi diagrams of DPPE-TR localizations in DiPhyPC bilayers at 14 °C (B) without and (C) with aggregates removed. (D) Spatial autocorrelations of localizations with increasing p_{th} (*arrow*). (E) The localizations per aggregate (N) and the resulting fraction of localizations removed are shown upon increasing p_{th}. The greatest p_{th} value that yielded $N \leq 3$ (*star*) was used for aggregate-free analysis. (F) MSD versus Δt is shown for DPPE-TR in DiPhyPC SLBs with and without aggregates included at 14 °C and 28 °C. Error bars represent the standard error from at least three repeated measurements. (A-C) Scale bars, 1 μm.

Aggregates appeared in all DiPhyPC-containing membranes (*i.e.,* 1:0:0, 1:1:2, and 2:2:1) and with a greater abundance when the tie-line between coexisting phases was presumably longer (Fig. 4). As the temperature was increased, the number of aggregates present on the membrane decreased. As the cholesterol concentration in the membrane was increased, the number of aggregates present on the membrane increased. There was no significant difference in aggregation between L_d and L_o phases.

3.4. Diffusion versus phase

D_{MSD} and D_{RD} after aggregate removal were measured for all membrane compositions and temperatures (Table S1). The diffusion difference between the L_d and L_o phases was greater for membranes with less cholesterol in which the tie-lines were presumably longer. For example, D_{MSD} from the L_d phase was (1.8 ± 0.6)x greater than that of the L_o phase at both 14 °C and 28 °C for 2:2:1 SLBs (Fig. 5A). The higher cholesterol, 1:1:2 SLBs displayed no significant difference in D_{MSD} from the L_d and L_o phases while tie-lines were presumably short (Fig. 5B).

3.5. Single-particle tracking versus FCS

FCS provides a measure of single-lipid diffusion averaged over a diffraction-limited spot of 200 nm diameter. Because the phases diffuse slowly on SLBs, a location on the SLB could be assessed by diffraction-limited fluorescence imaging to be L_d, L_o, or a homogeneous L phase before performing FCS. FCS revealed the diffusion of DPPE-TR to be 2x faster for POPC than DiPhyPC SLBs; D_{FCS} = 4.9 ± 0.2 μm^2/s and 2.5 ± 0.8 μm^2/s, respectively (Table S2). D_{FCS} was faster for the L_d versus L_o phases, although not significantly for the cholesterol-rich 1:1:2 SLB; D_{FCS} was (1.6 ± 0.5)x faster for L_d versus L_o phases in the 2:2:1 SLBs and (1.1 ± 0.4)x for the 1:1:2 SLBs. This result consistently demonstrates that a greater difference in diffusion between the L_d and L_o phases occurs for a membrane that has less cholesterol and, presumably, a longer tie-line.

3.6. Diffusion versus temperature

Increasing the sample temperature increased the speed of the single-lipid diffusion in all tested conditions (Fig. 6). The diffusion coefficient versus temperature was fit by a free area model derived from the kinetic theory of gas, which assumes that diffusion occurs when lipids hop to a surrounding transient void or free area that is created by a thermal density fluctuation (Galla et al., 1979). Since lipid hopping is an activated process dominated by van der Waal's interactions, activation energy (E_A) represents the energy barrier to be overcome for hopping between initial and final states that limit the molecular-scale lipid

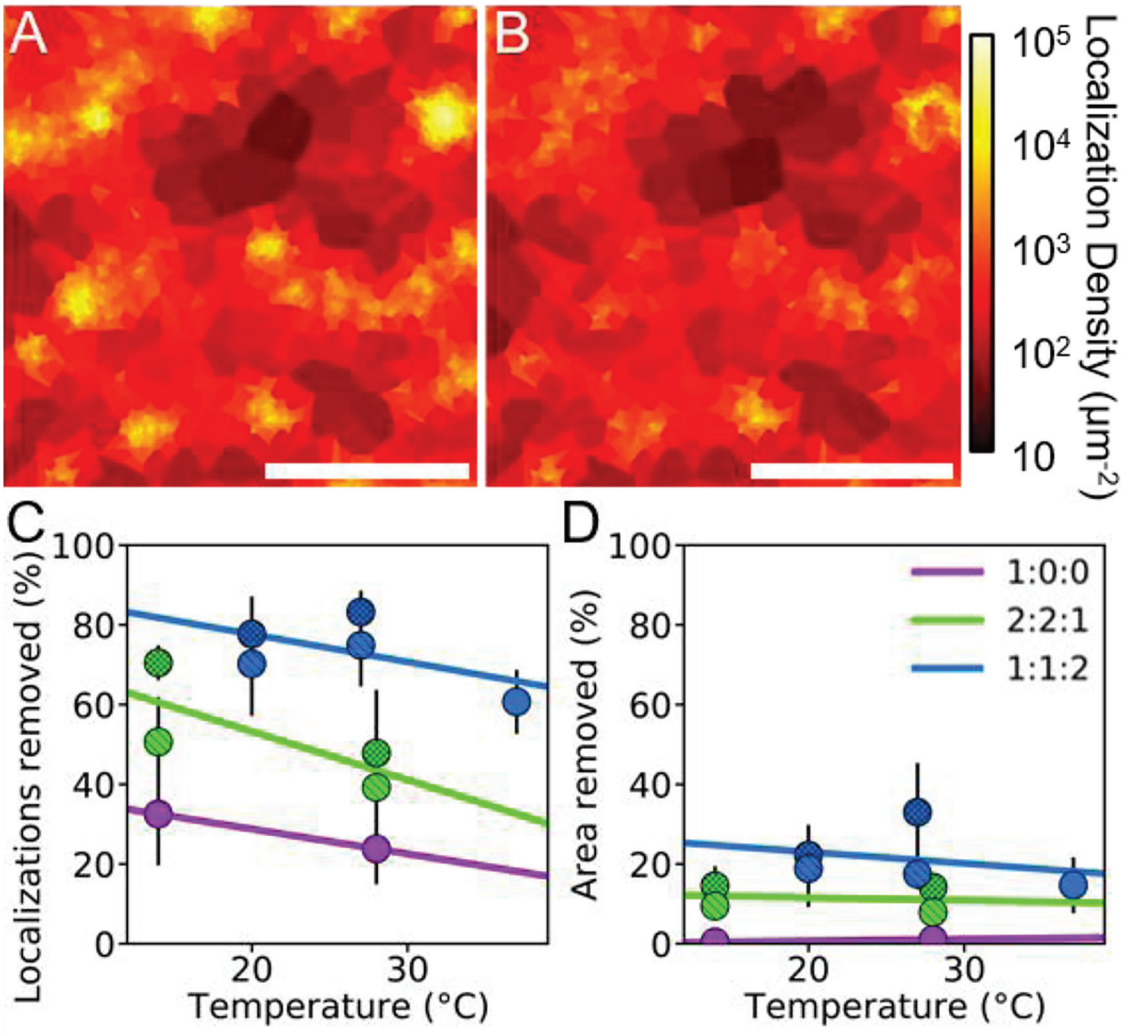

Fig. 4. Aggregates were present in SLBs with DiPhyPC. Representative Voronoi diagrams of DPPE-TR localizations in the L_d phase SLBs of 1:1:2 molar ratios of DiPhyPC:DPPC:cholesterol at 20 °C (A) without and (B) with aggregates removed. Scale bars, 0.5 μm. The fraction of the removed (C) localizations and (D) SLB area shows more aggregates were removed when the tie-lines were presumably longer. Marker hatching indicates the lipid phase: backslash = L_o; crosshatching = L_d; empty = L or L_α. Linear fits are shown to guide the eye. Error bars represent the standard error of at least three repeated measurements.

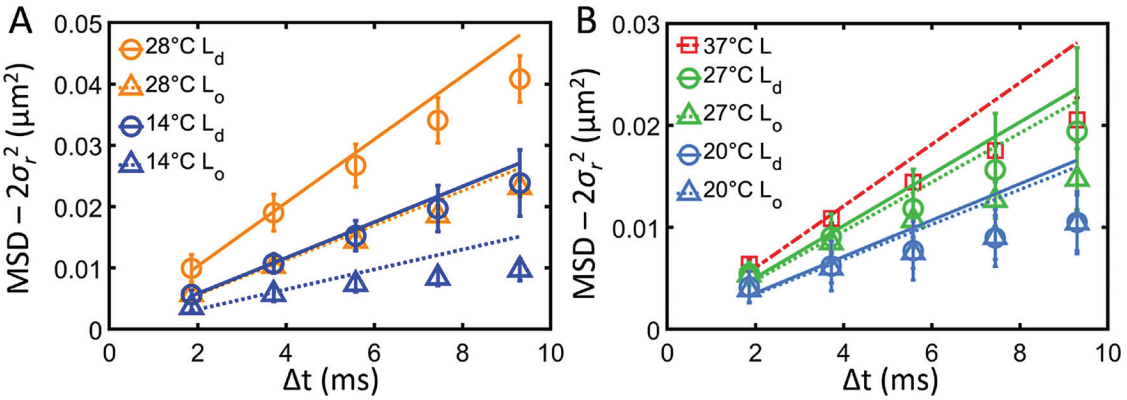

Fig. 5. MSD versus Δt for (A) 2:2:1 and (B) 1:1:2 molar ratios of DiPhyPC:DPPC:cholesterol SLBs demonstrate the importance of temperature and phase in single-lipid diffusion. The measured MSD values were corrected by the localization uncertainty reported by ThunderSTORM (σ_r) such that the resulting linear fits have a y-intercept of zero. Fits were performed for short time steps (Δt = 1.9-3.8 ms). Error bars represent the standard error of the means with at least three repeats.

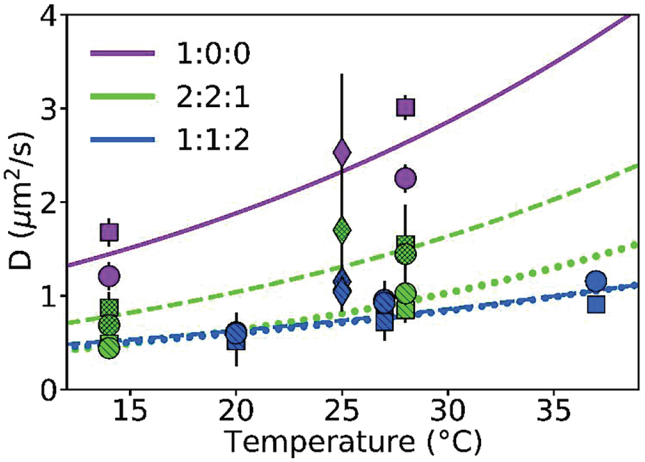

Fig. 6. The diffusion of DPPE-TR was measured with varying membrane composition, lipid phase, temperature, and measurement technique. The color indicates the DiPhyPC:DPPC:cholesterol molar ratios. The marker shape indicates the measurement technique: square = D_{MSD}; circle = D_{RD}; diamond = D_{FCS}. The marker hatching indicates the lipid phase: backslash = L_o; cross-hatching = L_d; empty = L *or* L_α. Fits of Eq. 7 are shown for each phase (Table S3). Error bars represent the standard error of repeated measurements with at least three repeats.

translation (Filippov et al., 2003; Macedo and Litovitz, 1965; Vaz et al., 1985). Thus, the diffusion coefficient versus temperature can be described by the Arrhenius equation,

$$D = D_0 \exp\left(-\frac{E_A}{RT}\right) \quad (7)$$

D_0 represents the diffusion rate at high temperatures. Fitting this exponential yielded temperature-independent values for E_A and D_0 that are consistent with prior studies (Fig. 6 and Table S3).

4. Discussion

4.1. Phase separation on SLBs

Unlike domains on GUVs, all optically resolvable lipid domains in SLBs were immobile on the time scale of our experiments (<2 h). The interaction between the glass substrate and the SLB was too strong for the domains to move or coalescence, consistent with previous observations (Gunderson and Honerkamp-Smith, 2018). The immobile domains were convenient for correlating single-lipid diffusion with the phases due to the minimal diffusion of the phase boundary during SPT data acquisition; however, single-lipid diffusion itself is also affected by the membrane-substrate interaction. Lipids in GUVs diffuse 3x faster than lipids in SLBs (Beckers et al., 2020), and DPPE-TR only in the top leaflet was (1.2 ± 0.1)x faster than when in both leaflets (Woodward et al., 2018). If there was an equal contribution from DPPE-TR in both leaflets of the SLB, then the DPPE-TR in the top leaflet diffused 1.5x faster than DPPE-TR in the bottom leaflet.

Regardless of the initial domain distribution, we did not observe large domains (radius > 1 μm) form upon cooling well-mixed SLBs. The domains from well-mixed SLBs grew in size to near the diffraction-limited imaging resolution. The domains were clearly present, but their sizes were difficult to determine due to both optical blurring and their non-circular shape. Additionally, substrate-membrane interactions affect T_m with a leaflet and lipid-type dependency such that not all lipids were well mixed after heating even when a uniform fluorescence emission was observed (Gunderson and Honerkamp-Smith, 2018). This effect may be amplified when Ca^{2+} is present and lipid pinning sites occur.

By decreasing the rate of sample temperature changes and increasing the duration at warm temperatures, we observed a reduced correlation of domain locations upon thermal cycling, as shown previously (Stanich et al., 2013). Additionally, the surface roughness of the substrate may have increased the domain nucleation rate, resulting in nanoscale domains present across the membrane instead of macroscale domains forming by gradual accretion. This hypothesis is consistent with the prior observation that SLB phase domains on glass or roughened mica were orders of magnitude smaller than on smooth mica; the membrane domain size was more correlated to substrate roughness rather than the substrate surface chemistry (Goodchild et al., 2019).

We note that our results map to the phase-separating tie-line length is correlative and that we do not measure the tie-line directly in this study. Our analysis assumes that coexisting lipid phases with less cholesterol or in colder samples demonstrate a greater tie-line length (Fig. 1B), as established previously by direct measurement (Chiang et al., 2005; Veatch et al., 2006). We consider the tie-line length throughout this manuscript because it provides a convenient intellectual framework for interpreting many of our results.

4.2. Causes of lipid aggregation

As described above, lipid aggregation may occur due to a variety of mechanisms. For example, rhodamine-labeled lipids form oligomers and grow into nanodomains due to the interactions of their extended aromatic moiety (Jan Akhunzada et al., 2019), which may be enhanced by membrane curvature (Woodward et al., 2018). The Texas Red-labeled lipids used here are similar in fluorophore structure with

rhodamine-labeled lipids. Additionally, the saturated acyl tails of the DPPE-TR has been correlated with nanodomains within extended lipid phases (Sodt et al., 2014; Wu et al., 2016).

The exposure of a sample to light may induce phase separations via lipid peroxidation that is accelerated by fluorophores (Ayuyan and Cohen, 2006; Zhao et al., 2007). For example, some fluorophores such as Bodipy, DiO, DiI, Texas Red, and napthopyrene cause light-induced chemical changes to the lipids, including the oxidization of the unsaturated acyl tails (Zhao et al., 2007). Accordingly, DiPhyPC is frequently used for fluorescence-based diffusion studies because it provides a highly disordered acyl structure without carbon-carbon double bonds and resists light-induced chemical changes (Lindsey et al., 1979). DPPE-TR and light-induced aggregates are non-linearly dependent on the DPPE-TR concentration. Domain formation was 50x faster when 0.8 mol% rather than 0.15 mol% DPPE-TR was present (Zhao et al., 2007). The 15 mW of 561 nm wavelength light used here for 3 min of observation in the presence of 0.1 mol% DPPE-TR would be sufficient to cause light-induced alterations to the membrane phase behavior in the presence of unsaturated phospholipids. Our use of DiPhyPC was intended to minimize these light effects.

Lipid aggregates were previously seen more abundant in L_o domains (Wu et al., 2016), yet no correlation between lipid phases and aggregation was observed here. In both the 1:1:2 and 2:2:1 SLBs, there was no difference in the aggregation between the L_d and L_o phases. However, the 1:1:2 SLBs demonstrated greater aggregation than the 2:2:1 SLBs at all temperatures (Fig. 4). Aggregate formation is complex and depends on many factors. For example, the cause of the greater aggregation in the DiPhyPC versus POPC bilayers, as shown here, is of unknown and worthy of further examination.

4.3. Diffusion of lipid aggregates

Single-lipid diffusion provides a detailed examination of the behavior of individual molecules with the possibility to resolve variations between diffusion modes, sample heterogeneity, and non-Brownian behaviors. Confined single-molecule trajectories were observed here coincident with lipid aggregates. When single-particle tracking was previously performed with long trajectories (*i.e.,* over 100 steps per trajectory), the downward curvature of the MSD versus Δt, local variations in the diffusion rate, or transient spatial confinement was directly observed to reveal aggregation (Simson et al., 1995; Wu et al., 1977). Trajectories of fewer steps are amendable to detecting aggregates through analysis of the histogram of single-step lengths and fitting to a sum of Rayleigh distributions (Eq. 4). Aggregates displayed shorter step lengths than freely diffusing lipids, and the histogram of step lengths was fit best when multiple diffusers are assumed to be present (Spillane et al., 2014). Multiple-population fitting can yield the relative speed and abundance of each type of diffuser; however, single-step analysis requires each population to be >5% of the total and provide >10x difference in diffusion rates for reliable separation of the populations based on the tracer lipid trajectories. Since the aggregates observed here did not meet these criteria, we alternatively relied on the varying localization rate for aggregates versus the surrounding SLB to identify and exclude the aggregates from further analysis.

4.4. Resolution of Rayleigh distribution versus MSD analyses

MSD and Rayleigh distribution analyses provided varying precision in revealing the spatial resolution of diffusion differences. The MSD analysis typically provides greater accuracy in finding D, distributions in D from heterogeneous populations of diffusers, and inherently corrects for the localization uncertainty when not assuming MSD = 0 when Δt = 0. However, MSD analyses typically do not account for when one diffuser switches between diffusion modes or translates across a heterogeneous sample. Rayleigh distribution analyses, however, provide improved resolution in spatially varying D, assuming the single-particle trajectories are dense. For example, Rayleigh distribution analyses have been used to reveal the diffusion in 25 nm bins surrounding nanoscale membrane curvature (Kabbani et al., 2017; Kabbani and Kelly, 2017a; Woodward et al., 2018; Woodward and Kelly, 2020).

To demonstrate the tradeoff between spatial resolution and precision in determining D, we considered a hypothetical diffuser measured by SPT with varying analysis methods. If a Brownian diffuser of $D = 1\ \mu m^2/s$ was tracked for 1 s, then the diffuser would be expected to traverse 2 μm, which would result in an averaging of spatial variations in diffusion across this distance for a typical single-molecule MSD analysis. However, spatial resolution from Rayleigh distribution analysis depends on the acquisition frame rate and the length of each step with an inherent averaging over this length. If the acquisition occurs at 100 Hz, then the step length and spatial resolution would be for Rayleigh distribution analysis would be 200 nm. This example demonstrates a 10x improvement in spatial resolution for Rayleigh distribution versus MSD analysis. For short trajectories, such those used in this study, the MSD from each trajectory has large uncertainty; combining the trajectories from multiple molecules is necessary for accurate diffusion measurements for either MSD or Rayleigh distribution analysis, which further reduces the benefits of the MSD analysis.

The certainty with which D is determined can be approximated through statistical considerations. Both Rayleigh distribution and MSD analyses are Poisson noise-dominated processes such that the certainty in D is inversely proportional to the square root of the number of steps analyzed. Any gains in the area spatial resolution are matched by a proportional decrease in precision determining D. Unlike traditional MSD analyses, Rayleigh distribution fitting can be performed by averaging the step lengths over a user-defined area of the sample with this tradeoff in mind.

4.5. Comparison between D_{MSD}, D_{RD}, and D_{FCS}

D_{MSD} and D_{RD} were compared for all membrane composition, temperature, and phases (Fig. 6). D_{MSD} and D_{RD} varied by 18 ± 9%, which is typically within the experimental uncertainty for measuring the diffusion coefficient by any single method. D_{MSD} and D_{RD} displayed consistent trends in comparing lipid phases and varying temperatures. There were consistent differences between D_{MSD} and D_{RD} that depended on the rate of diffusion. Typically, when D_{MSD} was $> 1\ \mu m^2/s$, D_{MSD} was 1.2 ± 0.1 times larger than D_{RD}, and otherwise D_{MSD} was less than D_{RD}. This systematic variation between D_{MSD} and D_{RD} remains unexplained but could be a coincidence in our analyses.

Confocal FCS consistently provides a resolution consistent with the diffraction limit (*i.e.,* 200 nm), but is highly limited by the insensitive detection of subpopulations. D_{FCS} of DPPE-TR in POPC was 1.5 ± 0.5 times faster than D_{MSD} and D_{RD} (Tables S1 and S2). Commonly, FCS reports faster diffusion than SPT studies because D_{FCS} does not incorporate immobile or highly confined diffusive subpopulations, whereas SPT typically does. Even after aggregate removal, SPT yields slower diffusion than FCS, but the differences were within the measurement uncertainty of D.

4.6. Diffusion differences between lipid phases

When the tie-line between coexisting phases was longer, the difference between their diffusion was greater. The high cholesterol and short tie-line 1:1:2 SLBs displayed no significant difference in the diffusion rate between the L_d and L_o phases. However, the L_d phase of 2:2:1 SLBs displayed diffusion twice as fast as the L_o in 1:1:2 SLBs. The L_o phases in the 1:1:2 and 2:2:1 SLBs did not display significantly different diffusion. Accordingly, increasing cholesterol content slowed the diffusion coefficient for the L_d phase but not the L_o phase. This is in contrast to ternary mixtures of dioleoyl-phosphatidylcholine, sphingomyelin, and cholesterol that display greater cholesterol content is correlated with slower diffusion in the L_o phases and minimally changes in L_d phase (Kahya

et al., 2003; Scherfeld et al., 2003).

The 2:2:1 SLBs displayed faster DPPE-TR diffusion in L_d versus L_o at ratios similar to seen previously (Dietrich et al., 2001). When the cholesterol content increased to 50 % of the bilayer (*i.e.*, in 1:1:2 SLBs), the difference between tracer diffusion in the L_d and L_o phases became indistinguishable for all tested temperatures. This is consistent with prior work that showed single population diffusion on GUVs when the increasing cholesterol content (Scherfeld et al., 2003).

4.7. Temperature affects diffusion

The diffusion of DPPE-TR was faster at higher temperatures for all compositions tested, similar to as shown previously (Bag et al., 2014; Filippov et al., 2004; Sengupta et al., 2008; Tamm, 1988). The changes in D with temperature was robust to SLB composition or phase. The data acquired here were not sufficient to significantly distinguish between the D_0 and E_a values of each composition (Table S3). However, it is interesting to note that the E_a for the L_o phase was (1.07 ± 0.03)x higher than the L_d phase for both the 1:1:2 and 2:2:1 SLBs. Similarly, the E_a values for the 1:1:2 SLBs were (1.5 ± 0.8)x higher than the 2:2:1 SLBs. These results make intuitive sense in that a greater barrier exists for lipids to exchange locations in a L_o versus L_d phases or with a higher cholesterol content.

5. Conclusions

This manuscript reports the effects of lipid composition, phase, temperature, and data analysis procedures on the single-lipid diffusion in model membranes. The expected tie-line length separating coexisting liquid phases was correlated with the differences between the L_d and L_o phases. Single-lipid diffusion was consistently faster at higher temperatures and was consistent with a free area model for diffusion in which higher cholesterol and ordered phases resulted in greater activation energy for lateral lipid diffusion. DiPhyPC-containing membranes displayed nanoscale fluorescent lipid aggregation in both L_o and L_d phases. Increasing cholesterol and decreasing temperature both correlated with greater aggregation. However, there was no significant correlation between the lipid phases and aggregation. We report on methods for culling the aggregates and focusing on the mobile tracer lipids for SPT via MSD and Rayleigh distribution analyses. MSD analyses may provide for greater resolution of single-particle diffusion rates, but Rayleigh distribution analyses yield improved spatial resolution of diffusion rates in heterogeneous samples. The aggregate culling via localization rate thresholding provided consistency between SPT and FCS measurements of tracer lipid diffusion while measuring the compositional and temperature dependencies in lipid mobility.

Declaration of Competing Interest

The authors report no declarations of interest.

Acknowledgments

The authors thank Aurelia R. Honerkamp-Smith for valuable discussions. Financial support was provided by Thomas C. Rumble university graduate fellowship, Wayne State University summer dissertation award, and Richard J. Barber. This material is based upon work supported by the National Science Foundation under grant no. DMR-1652316.

Appendix A. Supplementary data

Supplementary material related to this article can be found, in the online version, at doi:https://doi.org/10.1016/j.chemphyslip.2020.104991.

References

Ackerman, D.G., Feigenson, G.W., 2015. Lipid bilayers: clusters, domains and phases. Essays Biochem. 57, 33–42. https://doi.org/10.1042/bse0570033.
Almeida, P.F.F., Vaz, W.L.C., Thompson, T.E., 1992. Lateral diffusion and percolation in two-phase, two-component lipid bilayers. Topology of the solid-phase domains in-plane and across the lipid bilayer. Biochemistry 31, 7198–7210. https://doi.org/10.1021/bi00146a024.
Ayuyan, A.G., Cohen, F.S., 2006. Lipid peroxides promote large rafts: effects of excitation of probes in fluorescence microscopy and electrochemical reactions during vesicle formation. Biophys. J. 91, 2172–2183. https://doi.org/10.1529/biophysj.106.087387.
Bag, N., Yap, D.H.X., Wohland, T., 2014. Temperature dependence of diffusion in model and live cell membranes characterized by imaging fluorescence correlation spectroscopy. Biochim. Biophys. Acta 1838, 802–813. https://doi.org/10.1016/j.bbamem.2013.10.009.
Baumgart, T., Hess, S.T., Webb, W.W., 2003. Imaging coexisting fluid domains in biomembrane models coupling curvature and line tension. Nature 425, 821–824. https://doi.org/10.1038/nature02013.
Beckers, D., Urbancic, D., Sezgin, E., 2020. Impact of nanoscale hindrances on the relationship between lipid packing and diffusion in model membranes. J. Phys. Chem. B. https://doi.org/10.1021/acs.jpcb.0c00445.
Berglund, A.J., 2010. Statistics of camera-based single-particle tracking. Phys. Rev. E 82, 011917. https://doi.org/10.1103/PhysRevE.82.011917.
Bleecker, J.V., Cox, P.A., Foster, R.N., Litz, J.P., Blosser, M.C., Castner, D.G., Keller, S.L., 2016. Thickness mismatch of coexisting liquid phases in non-canonical lipid bilayers. J. Phys. Chem. B 120, 2761–2770. https://doi.org/10.1021/acs.jpcb.5b10165.
Cheney, P.P., Weisgerber, A.W., Feuerbach, A.M., Knowles, M.K., 2017. Single lipid molecule dynamics on supported lipid bilayers with membrane curvature. Membranes (Basel) 7. https://doi.org/10.3390/membranes7010015.
Chiang, Y.-W., Zhao, J., Wu, J., Shimoyama, Y., Freed, J.H., Feigenson, G.W., 2005. New method for determining tie-lines in coexisting membrane phases using spin-label ESR. Biochim. Biophys. Acta 1668, 99–105. https://doi.org/10.1016/j.bbamem.2004.11.010.
Chiantia, S., Kahya, N., Ries, J., Schwille, P., 2006a. Effects of ceramide on liquid-ordered domains investigated by simultaneous AFM and FCS. Biophys. J. 90, 4500–4508. https://doi.org/10.1529/biophysj.106.081026.
Chiantia, S., Ries, J., Kahya, N., Schwille, P., 2006b. Combined AFM and two-focus SFCS study of raft-exhibiting model membranes. Chemphyschem 7, 2409–2418. https://doi.org/10.1002/cphc.200600464.
Coker, H.L.E., Cheetham, M.R., Kattnig, D.R., Wang, Y.J., Garcia-Manyes, S., Wallace, M. I., 2019. Controlling anomalous diffusion in lipid membranes. Biophys. J. 116, 1085–1094. https://doi.org/10.1016/j.bpj.2018.12.024.
Dietrich, C., Bagatolli, L.A., Volovyk, Z.N., Thompson, N.L., Levi, M., Jacobson, K., Gratton, E., 2001. Lipid rafts reconstituted in model membranes. Biophys. J. 80, 1417–1428.
Dimova, R., 2014. Recent developments in the field of bending rigidity measurements on membranes. In: Advances in Colloid and Interface Science, Special Issue in Honour of Wolfgang Helfrich, 208, pp. 225–234. https://doi.org/10.1016/j.cis.2014.03.003.
Feigenson, G.W., 2006. Phase behavior of lipid mixtures. Nat. Chem. Biol. 2, 560–563. https://doi.org/10.1038/nchembio1106-560.
Feigenson, G.W., 2009. Phase diagrams and lipid domains in multicomponent lipid bilayer mixtures. Biochim. Biophys. Acta 1788, 47–52. https://doi.org/10.1016/j.bbamem.2008.08.014.
Fessler, M.B., Parks, J.S., 2011. Intracellular lipid flux and membrane microdomains as organizing principles in inflammatory cell signaling. J. Immunol. 187, 1529–1535. https://doi.org/10.4049/jimmunol.1100253.
Filippov, A., Orädd, G., Lindblom, G., 2003. The effect of cholesterol on the lateral diffusion of phospholipids in oriented bilayers. Biophys. J. 84, 3079–3086.
Filippov, A., Orädd, G., Lindblom, G., 2004. Lipid lateral diffusion in ordered and disordered phases in raft mixtures. Biophys. J. 86, 891–896. https://doi.org/10.1016/S0006-3495(04)74164-8.
Galla, H.-J., Hartmann, W., Theilen, U., Sackmann, E., 1979. On two-dimensional passive random walk in lipid bilayers and fluid pathways in biomembranes. J. Membrain Biol. 48, 215–236. https://doi.org/10.1007/BF01872892.
Goodchild, J.A., Walsh, D.L., Connell, S.D.A., 2019. Nanoscale substrate roughness hinders domain formation in supported lipid bilayers. Langmuir. https://doi.org/10.1021/acs.langmuir.9b01990.
Gracià, R.S., Bezlyepkina, N., Knorr, R.L., Lipowsky, R., Dimova, R., 2010. Effect of cholesterol on the rigidity of saturated and unsaturated membranes: fluctuation and electrodeformation analysis of giant vesicles. Soft Matter 6, 1472–1482. https://doi.org/10.1039/B920629A.
Gunderson, R.S., Honerkamp-Smith, A.R., 2018. Liquid-liquid phase transition temperatures increase when lipid bilayers are supported on glass. In: Biochimica et Biophysica Acta (BBA) - Biomembranes, Emergence of Complex Behavior in Biomembranes, 1860, pp. 1965–1971. https://doi.org/10.1016/j.bbamem.2018.05.001.
Guo, S.-M., He, J., Monnier, N., Sun, G., Wohland, T., Bathe, M., 2012. Bayesian approach to the analysis of fluorescence correlation spectroscopy data II: application to simulated and in vitro data. Anal. Chem. 84, 3880–3888. https://doi.org/10.1021/ac2034375.
Harwardt, M.-L.I.E., Dietz, M.S., Heilemann, M., Wohland, T., 2018. SPT and imaging FCS provide complementary information on the dynamics of plasma membrane molecules. Biophys. J. 114, 2432–2443. https://doi.org/10.1016/j.bpj.2018.03.013.
Heberle, F.A., Feigenson, G.W., 2011. Phase separation in lipid membranes. Cold Spring Harb. Perspect. Biol. 3 https://doi.org/10.1101/cshperspect.a004630.

Hsieh, C.-L., Spindler, S., Ehrig, J., Sandoghdar, V., 2014. Tracking single particles on supported lipid membranes: multimobility diffusion and nanoscopic confinement. J. Phys. Chem. B 118, 1545–1554. https://doi.org/10.1021/jp412203t.

Hurley, J.H., Boura, E., Carlson, L.-A., Rózycki, B., 2010. Membrane budding. Cell 143, 875–887. https://doi.org/10.1016/j.cell.2010.11.030.

Jacobson, K., Hou, Y., Derzko, Z., Wojcieszyn, J., Organisciak, D., 1981. Lipid lateral diffusion in the surface membrane of cells and in multibilayers formed from plasma membrane lipids. Biochemistry 20, 5268–5275. https://doi.org/10.1021/bi00521a027.

Jan Akhunzada, M., D'Autilia, F., Chandramouli, B., Bhattacharjee, N., Catte, A., Di Rienzo, R., Cardarelli, F., Brancato, G., 2019. Interplay between lipid lateral diffusion, dye concentration and membrane permeability unveiled by a combined spectroscopic and computational study of a model lipid bilayer. Sci. Rep. 9, 1508. https://doi.org/10.1038/s41598-018-37814-x.

Jaqaman, K., Loerke, D., Mettlen, M., Kuwata, H., Grinstein, S., Schmid, S.L., Danuser, G., 2008. Robust single-particle tracking in live-cell time-lapse sequences. Nat Meth 5, 695–702. https://doi.org/10.1038/nmeth.1237.

Kabbani, A.M., Kelly, C.V., 2017a. The detection of nanoscale membrane bending with polarized localization microscopy. Biophys. J. 113, 1782–1794. https://doi.org/10.1016/j.bpj.2017.07.034.

Kabbani, A.M., Kelly, C.V., 2017b. Nanoscale membrane budding induced by CTxB and detected via polarized localization microscopy. Biophys. J. 113, 1795–1806. https://doi.org/10.1016/j.bpj.2017.08.031.

Kabbani, A.M., Woodward, X., Kelly, C.V., 2017. Revealing the effects of nanoscale membrane curvature on lipid mobility. Membranes 7, 60. https://doi.org/10.3390/membranes7040060.

Kabbani, A.M., Raghunathan, K., Lencer, W.I., Kenworthy, A.K., Kelly, C.V., 2020. Structured clustering of the glycosphingolipid GM1 is required for membrane curvature induced by cholera toxin. Proc. Natl. Acad. Sci. U. S. A. 117, 14978–14986. https://doi.org/10.1073/pnas.2001119117.

Kahya, N., Scherfeld, D., Bacia, K., Poolman, B., Schwille, P., 2003. Probing lipid mobility of raft-exhibiting model membranes by fluorescence correlation spectroscopy. J. Biol. Chem. 278, 28109–28115. https://doi.org/10.1074/jbc.M302969200.

Kiessling, V., Yang, S.-T., Tamm, L.K., 2015. Supported lipid bilayers as models for studying membrane domains. Curr. Top. Membr. 75, 1–23. https://doi.org/10.1016/bs.ctm.2015.03.001.

Knight, J.D., Lerner, M.G., Marcano-Velázquez, J.G., Pastor, R.W., Falke, J.J., 2010. Single molecule diffusion of membrane-bound proteins: window into lipid contacts and bilayer dynamics. Biophys. J. 99, 2879–2887. https://doi.org/10.1016/j.bpj.2010.08.046.

Kollmitzer, B., Heftberger, P., Podgornik, R., Nagle, J.F., Pabst, G., 2015. Bending rigidities and interdomain forces in membranes with coexisting lipid domains. Biophys. J. 108, 2833–2842. https://doi.org/10.1016/j.bpj.2015.05.003.

Lagerholm, B.C., Andrade, D.M., Clausen, M.P., Eggeling, C., 2017. Convergence of lateral dynamic measurements in the plasma membrane of live cells from single particle tracking and STED-FCS. J. Phys. D Appl. Phys. 50, 063001 https://doi.org/10.1088/1361-6463/aa519e.

Lin, W.-C., Blanchette, C.D., Longo, M.L., 2007. Fluid-phase chain unsaturation controlling domain microstructure and phase in ternary lipid bilayers containing GalCer and cholesterol. Biophys. J. 92, 2831–2841. https://doi.org/10.1529/biophysj.106.095422.

Lindblom, G., Orädd, G., Filippov, A., 2006. Lipid lateral diffusion in bilayers with phosphatidylcholine, sphingomyelin and cholesterol: an NMR study of dynamics and lateral phase separation. Chemistry and Physics of Lipids, Protein:Lipid Interactions 141, 179–184. https://doi.org/10.1016/j.chemphyslip.2006.02.011.

Lindsey, H., Petersen, N.O., Chan, S.I., 1979. Physicochemical characterization of 1,2-diphytanoyl-sn-glycero-3-phosphocholine in model membrane systems. Biochim. Biophys. Acta 555, 147–167. https://doi.org/10.1016/0005-2736(79)90079-8.

Macedo, P.B., Litovitz, T.A., 1965. On the relative roles of free volume and activation energy in the viscosity of liquids. J. Chem. Phys. 42, 245–256. https://doi.org/10.1063/1.1695683.

McConnell, H.M., Radhakrishnan, A., 2003. Condensed complexes of cholesterol and phospholipids. Biochim. Biophys. Acta 1610, 159–173. https://doi.org/10.1016/s0005-2736(03)00015-4.

Ovesný, M., Křížek, P., Borkovec, J., Svindrych, Z., Hagen, G.M., 2014. ThunderSTORM: a comprehensive ImageJ plug-in for PALM and STORM data analysis and super-resolution imaging. Bioinformatics 30, 2389–2390. https://doi.org/10.1093/bioinformatics/btu202.

Pike, L.J., 2006. Rafts defined: a report on the keystone symposium on lipid rafts and cell function. J. Lipid Res. 47, 1597–1598. https://doi.org/10.1194/jlr.E600002-JLR200.

Pralle, A., Keller, P., Florin, E.-L., Simons, K., Hörber, J.K.H., 2000. Sphingolipid–Cholesterol rafts diffuse as small entities in the plasma membrane of mammalian cells. J. Cell Biol. 148, 997–1008.

Qian, H., Sheetz, M.P., Elson, E.L., 1991. Single particle tracking. Analysis of diffusion and flow in two-dimensional systems. Biophys. J. 60, 910–921.

Radhakrishnan, A., McConnell, H., 2005. Condensed complexes in vesicles containing cholesterol and phospholipids. Proc. Natl. Acad. Sci. U. S. A. 102, 12662–12666. https://doi.org/10.1073/pnas.0506043102.

Saxton, M.J., 1997. Single-particle tracking: the distribution of diffusion coefficients. Biophys. J. 72, 1744–1753.

Scherer, K.M., Spille, J.-H., Sahl, H.-G., Grein, F., Kubitscheck, U., 2015. The lantibiotic nisin induces lipid II aggregation, causing membrane instability and vesicle budding. Biophys. J. 108, 1114–1124. https://doi.org/10.1016/j.bpj.2015.01.020.

Scherfeld, D., Kahya, N., Schwille, P., 2003. Lipid dynamics and domain formation in model membranes composed of ternary mixtures of unsaturated and saturated phosphatidylcholines and cholesterol. Biophys. J. 85, 3758–3768. https://doi.org/10.1016/S0006-3495(03)74791-2.

Schindelin, J., Arganda-Carreras, I., Frise, E., Kaynig, V., Longair, M., Pietzsch, T., Preibisch, S., Rueden, C., Saalfeld, S., Schmid, B., Tinevez, J.-Y., White, D.J., Hartenstein, V., Eliceiri, K., Tomancak, P., Cardona, A., 2012. Fiji: an open-source platform for biological-image analysis. Nat. Methods 9, 676–682. https://doi.org/10.1038/nmeth.2019.

Sengupta, P., Hammond, A., Holowka, D., Baird, B., 2008. Structural determinants for partitioning of lipids and proteins between coexisting fluid phases in giant plasma membrane vesicles. Biochim. Biophys. Acta 1778, 20–32. https://doi.org/10.1016/j.bbamem.2007.08.028.

Shelby, S.A., Holowka, D., Baird, B., Veatch, S.L., 2013. Distinct stages of stimulated FcεRI receptor clustering and immobilization are identified through superresolution imaging. Biophys. J. 105, 2343–2354. https://doi.org/10.1016/j.bpj.2013.09.049.

Simons, K., Ikonen, E., 1997. Functional rafts in cell membranes. Nature 387, 569–572. https://doi.org/10.1038/42408.

Simons, K., Toomre, D., 2000. Lipid rafts and signal transduction. Nat. Rev. Mol. Cell Biol. 1, 31–39. https://doi.org/10.1038/35036052.

Simson, R., Sheets, E.D., Jacobson, K., 1995. Detection of temporary lateral confinement of membrane proteins using single-particle tracking analysis. Biophys. J. 69, 989–993. https://doi.org/10.1016/S0006-3495(95)79972-6.

Sodt, A.J., Sandar, M.L., Gawrisch, K., Pastor, R.W., Lyman, E., 2014. The molecular structure of the liquid-ordered phase of lipid bilayers. J. Am. Chem. Soc. 136, 725–732. https://doi.org/10.1021/ja4105667.

Spillane, K.M., Ortega-Arroyo, J., de Wit, G., Eggeling, C., Ewers, H., Wallace, M.I., Kukura, P., 2014. High-speed single-particle tracking of GM1 in model membranes reveals anomalous diffusion due to interleaflet coupling and molecular pinning. Nano Lett. 14, 5390–5397. https://doi.org/10.1021/nl502536u.

Stanich, C.A., Honerkamp-Smith, A.R., Putzel, G.G., Warth, C.S., Lamprecht, A.K., Mandal, P., Mann, E., Hua, T.-A.D., Keller, S.L., 2013. Coarsening dynamics of domains in lipid membranes. Biophys. J. 105, 444–454. https://doi.org/10.1016/j.bpj.2013.06.013.

Štefl, M., Šachl, R., Humpolíčková, J., Cebecauer, M., Macháň, R., Kolářová, M., Johansson, L.B.-Å., Hof, M., 2012. Dynamics and size of cross-linking-induced lipid nanodomains in model membranes. Biophys. J. 102, 2104–2113. https://doi.org/10.1016/j.bpj.2012.03.054.

Sun, H., Chen, L., Gao, L., Fang, W., 2015. Nanodomain formation of ganglioside GM1 in lipid membrane: effects of cholera toxin-mediated cross-linking. Langmuir 31, 9105–9114. https://doi.org/10.1021/acs.langmuir.5b01866.

Tamm, L.K., 1988. Lateral diffusion and fluorescence microscope studies on a monoclonal antibody specifically bound to supported phospholipid bilayers. Biochemistry 27, 1450–1457. https://doi.org/10.1021/bi00405a009.

Vaz, W.L.C., Clegg, R.M., Hallmann, D., 1985. Translational diffusion of lipids in liquid crystalline phase phosphatidylcholine multibilayers. A comparison of experiment with theory. Biochemistry 24, 781–786. https://doi.org/10.1021/bi00324a037.

Veatch, S.L., 2007. Electro-formation and fluorescence microscopy of giant vesicles with coexisting liquid phases. Methods Mol. Biol. 398, 59–72. https://doi.org/10.1007/978-1-59745-513-8_6.

Veatch, S.L., Keller, S.L., 2002. Organization in lipid membranes containing cholesterol. Phys. Rev. Lett. 89, 268101. https://doi.org/10.1103/PhysRevLett.89.268101.

Veatch, S.L., Keller, S.L., 2005. Seeing spots: complex phase behavior in simple membranes. In: Biochimica et Biophysica Acta (BBA) - Molecular Cell Research, Lipid Rafts: From Model Membranes to Cells, 1746, pp. 172–185. https://doi.org/10.1016/j.bbamcr.2005.06.010.

Veatch, S.L., Gawrisch, K., Keller, S.L., 2006. Closed-loop miscibility gap and quantitative tie-lines in ternary membranes containing diphytanoyl PC. Biophys. J. 90, 4428–4436. https://doi.org/10.1529/biophysj.105.080283.

Veatch, S.L., Machta, B.B., Shelby, S.A., Chiang, E.N., Holowka, D.A., Baird, B.A., 2012. Correlation functions quantify super-resolution images and estimate apparent clustering due to over-counting. PLoS One 7, e31457. https://doi.org/10.1371/journal.pone.0031457.

Wawrezinieck, L., Rigneault, H., Marguet, D., Lenne, P.-F., 2005. Fluorescence correlation spectroscopy diffusion laws to probe the submicron cell membrane organization. Biophys. J. 89, 4029–4042. https://doi.org/10.1529/biophysj.105.067959.

Woodward, X., Kelly, C.V., 2020. Coexisting lipid phases alter lipid dynamics and sort on nanoscale membrane curvature. bioRxiv 2020. https://doi.org/10.1101/2020.09.23.310086, 09.23.310086.

Woodward, X., Stimpson, E.E., Kelly, C.V., 2018. Single-lipid tracking on nanoscale membrane buds: the effects of curvature on lipid diffusion and sorting. In: Biochimica et Biophysica Acta (BBA) - Biomembranes, Emergence of Complex Behavior in Biomembranes, 1860, pp. 2064–2075. https://doi.org/10.1016/j.bbamem.2018.05.009.

Wu, E., Jacobson, K., Papahadjopoulos, D., 1977. Lateral diffusion in phospholipid multibilayers measured by fluorescence recovery after photobleaching. Biochemistry 16, 3936–3941. https://doi.org/10.1021/bi00636a034.

Wu, H.-M., Lin, Y.-H., Yen, T.-C., Hsieh, C.-L., 2016. Nanoscopic substructures of raft-mimetic liquid-ordered membrane domains revealed by high-speed single-particle tracking. Sci. Rep. 6, 20542. https://doi.org/10.1038/srep20542.

Yuan, C., Johnston, L.J., 2001. Atomic force microscopy studies of ganglioside GM1 domains in phosphatidylcholine and phosphatidylcholine/cholesterol bilayers. Biophys. J. 81, 1059–1069.

Yuan, C., Furlong, J., Burgos, P., Johnston, L.J., 2002. The size of lipid rafts: an atomic force microscopy study of ganglioside GM1 domains in sphingomyelin/DOPC/cholesterol membranes. Biophys. J. 82, 2526–2535.

Zhao, J., Wu, J., Shao, H., Kong, F., Jain, N., Hunt, G., Feigenson, G., 2007. Phase studies of model biomembranes: macroscopic coexistence of Lα + Lβ, with light-induced coexistence of Lα + Lo phases. Biochim. Biophys. Acta 1768, 2777–2786. https://doi.org/10.1016/j.bbamem.2007.07.009.